

Characterization of Polariton Dynamics in a Multimode Cavity: Noise-enhanced Ballistic Expansion

Ilia Tutunnikov ,^{1, 2,*} Md Qutubuddin ,^{3,*} H. R. Sadeghpour ,² and Jianshu Cao ,^{1, †}

¹*Department of Chemistry, Massachusetts Institute of Technology, Cambridge, Massachusetts 02139, USA*

²*ITAMP, Center for Astrophysics | Harvard & Smithsonian, Cambridge, Massachusetts 02138, USA*

³*Beijing Computational Science Research Center, Beijing 100193, China*

(Dated: October 16, 2024)

Advances in optical measurements enable precise tracking of cavity polariton dynamics with exceptional spatiotemporal resolution. Building on these developments, we present a comprehensive theoretical analysis of wave packet dynamics in a noisy emitter lattice embedded in a multi-mode microcavity. We uncover a series of dynamic phenomena in both the noise-free and noisy cases: (i) In the noise-free case, the emitters' probability density splits into two Gaussians whose group velocities are defined by the lower and upper polariton branches. (ii) Noise induces dephasing and leads to multiple dynamical stages with different time scales spanning several orders of magnitude. These stages include, in order of increasing duration: underdamped Rabi oscillations; damping of the center of mass velocity of the emitters' probability density; population thermalization; and the transition from the ballistic to the diffusive regimes of the probability density spreading. (iii) Most strikingly, dephasing enhances the ballistic spreading, which persists for several orders of magnitude longer than it does without a cavity. Some of our predictions align with recent experimental observations, while others can be tested in existing platforms. Understanding wave packet dynamics across multiple time scales in the presence of noise is crucial for optimizing polaritonic devices. This study paves the way for future experiments focused on light-matter interactions in complex systems.

I. INTRODUCTION

Strong light-matter interactions are promising for controlling and enhancing material properties and engineering novel devices. Cavities are especially effective for achieving a strong collective coupling between material excitations and cavity photons, giving rise to hybrid excitations termed cavity polaritons. Polaritons exhibit fascinating phenomena with important applications across photonics and materials science [1–3]. Over the past decade, pioneering experiments in cavity-based platforms have shown modifications to chemical dynamics and enhanced energy transfer [4–12], exciton [13–17] and charge transport [18–21]. These experimental advancements have led to the emergence of polaritonic chemistry as a new research field [22–24]. To complement the experimental breakthroughs, new theoretical models have been developed to account for the details of the emitters and complex environments [25, 26], allowing them to describe the subtleties of exciton-polariton systems [27–35].

Modern microscopy techniques allow tracking of the evolution of exciton-polariton wave packets with high spatial-temporal resolution [36–39]. These experiments motivate the theoretical analysis of polariton-mediated transport in multi-mode cavities. While single-mode models, like Dicke [40] and Tavis-Cummings (TC) [41], allow for simplified analyses, they predict that localized excitations can instantaneously travel to distant emitters, which is unphysical. In contrast, multi-mode models with

physical photonic dispersion satisfy the relativistic constraints [34, 35].

A comprehensive and rigorous treatment of polariton dynamics in multi-mode cavities is challenging due to the typically large number of emitters and cavity modes. Moreover, the complexities of realistic systems, including cavity losses, disorder, and environmental dephasing [42, 43], make accurate theoretical description even more demanding. The effects of static and dynamic disorder in polariton systems have been explored theoretically using various approaches, including perturbation theory [44, 45], exact diagonalization and integration [28, 35], mean-field-based approaches [46–48], and *ab initio* simulation [49, 50]. Despite these advancements, a complete dynamic picture covering all the stages of evolution is still lacking. This includes a detailed description of the transition between the ballistic and diffusive regimes of the wave packet expansion.

Here, we provide a complete analysis of the spatiotemporal dynamics of polariton wave packets in multi-mode cavities. We adopt the stochastic multi-mode TC model to incorporate both the continuum of photon modes and the stochastic dephasing noise acting on the emitters. This stochastic model is appropriate when the emitters are coupled to a thermal bath at a relatively high temperature. To make the analysis feasible, we consider an effectively one-dimensional (1D) microcavity with the embedded 1D lattice of identical emitters [35], as shown in Fig. 1. Although the emitters do not interact directly, their coupling to the cavity modes enables the propagation of excitonic wave packets.

The developed model presents methodological advancements and yields various experimentally relevant qualitative and quantitative predictions. The key find-

* These authors contributed equally to this work.

† jianshu@mit.edu

ings are summarized as follows:

1. Our quantum master equation enables efficient large-scale time-dependent simulations of multi-mode cavity systems where emitters are subject to noise. This lays the groundwork for future studies incorporating additional processes, such as cavity losses or direct inter-emitter interactions.
2. In the presence of noise, the emitters' probability density dynamics feature a sequence of stages across different time scales, forming a universal hierarchy. These stages include, in order of increasing duration: underdamped Rabi oscillations; damping of the center of mass velocity of the emitters' probability density; population thermalization; and the transition from the ballistic to the diffusive regimes of the probability density spreading.
3. Notably, despite the noise, the probability density expansion remains ballistic for several orders of magnitude longer than the dephasing time observed in a lattice with direct inter-emitter coupling in the absence of a cavity. Moreover, in the presence of noise, the rate of expansion is enhanced compared to the noise-free case.

The article is organized as follows. In Sec. II, we define the system Hamiltonian and discuss its eigenenergies and eigenstates. The noise-free wave packet dynamics are detailed in Sec. III, followed by an analysis of the dynamics with noise in Sec. IV. Finally, we summarize our findings and provide an outlook in Sec. V.

II. SYSTEM DEFINITION

We consider a 1D lattice of $N \gg 1$ identical, non-interacting emitters (two-level systems, TLS) with transition energy $\hbar\omega_{\text{eg}}$ embedded in effectively 1D cavity of length $L \equiv L_x$, i.e., multi-mode TC model (Fig. 1). Cavity mode frequencies are given by

$$\tilde{\omega}_k = \sqrt{c^2 \left(\frac{2\pi k}{L} \right)^2 + \tilde{\omega}_c^2}, \quad (1)$$

where k is an integer, c is the speed of light, and $\tilde{\omega}_c > 0$ arises due to the spatial confinement of the field in the y and z directions. Assuming the emitters are located at positions $r_n = nL/N$ (n is an integer, $-N/2 \leq n \leq N/2$), the system's Hamiltonian is given by [28, 35, 51]

$$\begin{aligned} \hat{H} = & \sum_k \hbar\tilde{\omega}_k |a_k\rangle\langle a_k| + \sum_{n=-N/2}^{N/2} \hbar\omega_{\text{eg}} |b_n\rangle\langle b_n| \\ & + \frac{\tilde{g}}{\sqrt{L}} \sum_{k,n} e^{i\frac{2\pi k}{L}r_n} |a_k\rangle\langle b_n| + \text{c.c.}, \end{aligned} \quad (2)$$

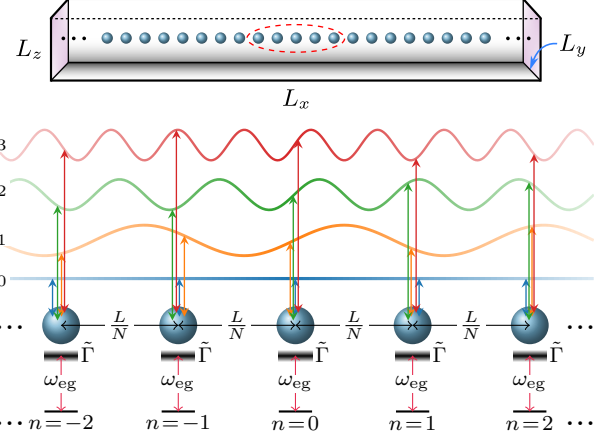


FIG. 1. Schematic illustration of the multi-mode TC model. N identical TLS emitters (blue spheres) are arranged in a 1D lattice along the x axis of an effectively 1D optical cavity of length $L \equiv L_x$ ($L_y, L_z \ll L_x$). The lower part shows the details of five example emitters in the center of the cavity. The transition energy is $\hbar\omega_{\text{eg}}$, while the lattice spacing is L/N . Emitters interact with cavity modes having energies $\tilde{\omega}_k$ given by Eq. (1). Here, only interactions between the example molecules and the modes with energies $\hbar\omega_0, \dots, \hbar\omega_3$ are shown for simplicity. Within the Haken-Strobl-Reineker model (see Sec. IV), the transition energy fluctuates about the average value ω_{eg} , and the fluctuations' autocorrelation function is $\tilde{\Gamma}\delta(t)$.

where $|a_k\rangle$ is the cavity state with a single excitation in photon mode k , $|b_n\rangle$ is the matter subsystem state with a single excited emitter at site n , and $\tilde{g} > 0$ is the matter-field coupling constant. Our analysis is restricted to the single excitation manifold.

Here, energy, length, frequency, and time are measured in units of $\hbar\omega_{\text{eg}}$, $\ell \equiv c/\omega_{\text{eg}}$, ω_{eg} , and $1/\omega_{\text{eg}}$ respectively. \hbar is set to unity in the expressions hereafter for convenience. Letting $L = M\ell$, the dimensionless mode frequency is given by

$$\omega_k = \sqrt{\left(\frac{2\pi k}{M} \right)^2 + \omega_c^2}, \quad (3)$$

where $\omega_c = \tilde{\omega}_c/\omega_{\text{eg}}$.

\hat{H} can be simplified using the Bloch states as the basis for the emitters' subsystem. The transformed dimensionless Hamiltonian is given by (see App. A for details)

$$\begin{aligned} \hat{H} = & \sum_{k=-N/2}^{N/2} (\omega_k |a_k\rangle\langle a_k| + |b_k\rangle\langle b_k|) \\ & + g \sum_{k=-N/2}^{N/2} (|a_k\rangle\langle b_k| + |b_k\rangle\langle a_k|), \end{aligned} \quad (4)$$

where $g = \tilde{g}\sqrt{\rho}/(\hbar\omega_{\text{eg}}\sqrt{\ell}) = \tilde{g}\sqrt{N/M}/(\hbar\omega_{\text{eg}}\sqrt{\ell})$ is the dimensionless collective coupling constant, and $\rho = N/M$

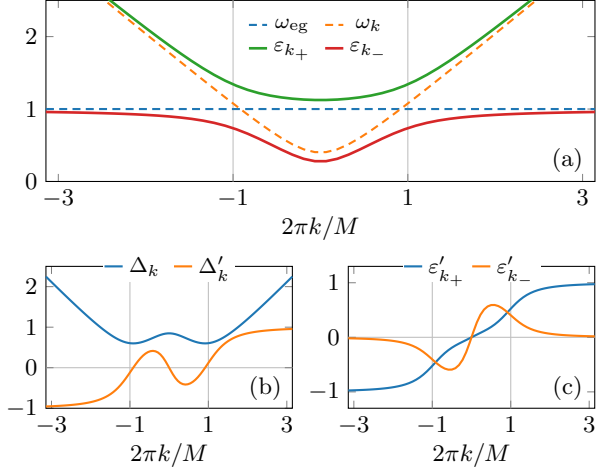


FIG. 2. (a) Upper and lower polariton branches [see Eqs. (3) and (6a)]. (b) VRS in Eq. (6b) and its derivative. (c) Group velocities, $\varepsilon'_{k\pm} \equiv d_k \varepsilon_{k\pm}$. Parameters: $\omega_c = 0.4$, $g = 0.3$ (strong coupling regime).

is the dimensionless number density. This form of \hat{H} reveals that the system can be viewed as a collection of TLSs, each describing the interaction between the k -th exciton and the k -th cavity mode. Throughout the paper, we set the number of cavity modes equal to the number of emitters, such that $-N/2 \leq k \leq N/2$.

The TLS eigenstates are the upper (+) and lower (−) polaritons

$$|v_{k\pm}\rangle = \begin{cases} -\sin(\theta_k) |a_k\rangle + \cos(\theta_k) |b_k\rangle, & +, \\ \cos(\theta_k) |a_k\rangle + \sin(\theta_k) |b_k\rangle, & -, \end{cases} \quad (5a)$$

$$\theta_k = \frac{1}{2} \arctan \left[\frac{2g}{\omega_k - \omega_{\text{eg}}} \right] + \frac{\pi}{2} \Theta(\omega_k - \omega_{\text{eg}}), \quad (5b)$$

where $\Theta(u) = 0$ when $u < 0$, and $\Theta(u) = 1$ when $u > 0$. The TLS eigenenergies, i.e., the polaritonic branches, are given by

$$\varepsilon_{k\pm} = \frac{\omega_k + \omega_{\text{eg}}}{2} \pm \frac{\Delta_k}{2}, \quad (6a)$$

$$\Delta_k \equiv \varepsilon_{k+} - \varepsilon_{k-} = \sqrt{4g^2 + (\omega_k - \omega_{\text{eg}})^2}, \quad (6b)$$

where Δ_k is the vacuum Rabi splitting (VRS) [see Fig. 2(a,b)].

III. DYNAMICS IN ISOLATED SYSTEM

We use a traveling Gaussian wave packet,

$$\psi_n(0) = \frac{1}{\sqrt{w\sqrt{\pi}}} \exp \left[-\frac{n^2}{2w^2} + ipn \right], \quad (7)$$

as the initial state of the matter subsystem, while the cavity modes are unpopulated at $t = 0$. Here, w is the

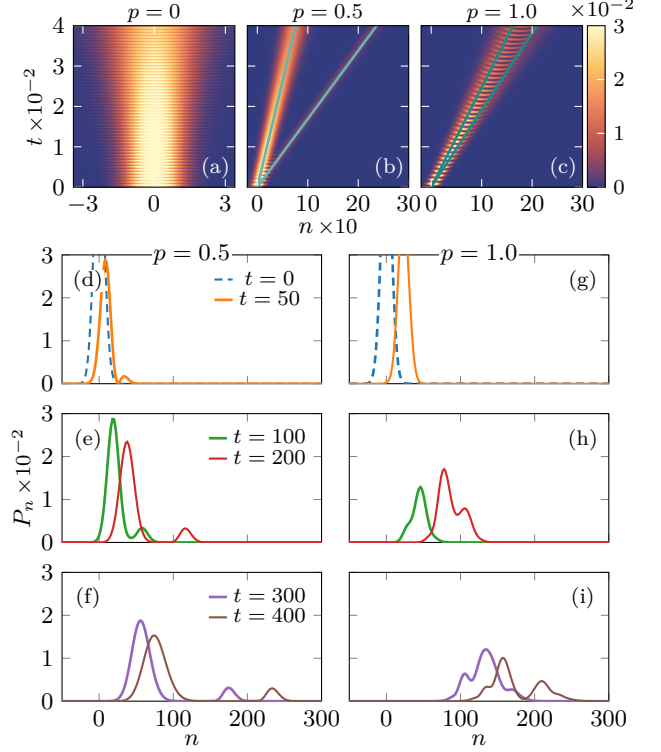


FIG. 3. (a-c) Unnormalized time-dependent emitters' population distribution, $P_n(t)$. The teal lines show the trajectories of the wave packets, $\psi_{n\pm}$. (d-i) $P_n(t)$ for $p = 0.5, 1.0$ at selected times. Parameters: $\omega_c = 0.4$, $g = 0.3$, $w = 10$.

dimensionless initial width of the Gaussian, and p is the initial dimensionless momentum (phase velocity). In k space, the initial probability density is given by

$$P_k(0) = \frac{w}{\sqrt{\pi}} \exp[-w^2(k - p)^2], \quad (8)$$

and the wider the sites' population distribution in the real space, the narrower is $P_k(0)$.

Invariance with respect to ρ . It is instructive to redefine k in Eq. (3), such that the dispersion relation becomes $\omega_k = \sqrt{(k\rho)^2 + \omega_c^2}$, and $-\pi \leq k \leq \pi$, accordingly. In the isolated system, observables are given by integrals involving a product of $P_k(0)$ and a function of the polaritonic energies $\varepsilon_{k\pm}$ in Eq. (6), i.e. $\int_{-\pi}^{\pi} P_k(0) f(\varepsilon_{k\pm}) dk$. Since $\varepsilon_{k\pm}$ depend on k only through ω_k , the results presented hereafter are invariant under the transformation of the initial state variables $w \rightarrow w\rho$ and $p \rightarrow p/\rho$. The observables remain invariant, assuming that the dimensionless collective coupling constant g is kept constant. Note that the spatial variable, n , must also be scaled by ρ .

Figure 3(a-c) shows the unnormalized time-dependent emitters' population distributions, $P_n(t) = |\psi_n(t)|^2$. The matter wave function is a sum of two wave packets associated with the upper and lower polaritons, $\psi_n(t) = \psi_{n+}(t) + \psi_{n-}(t)$ (see App. B for details). For the system

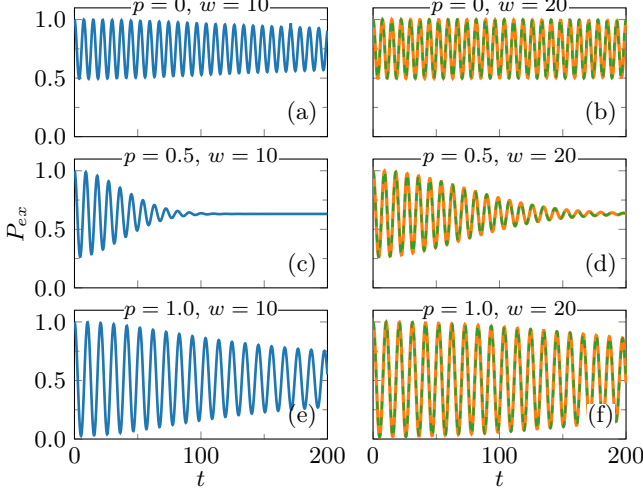


FIG. 4. Total excitonic population. The solid curves were obtained using the exact integral formula, while the dashed curves in panels (b,d,f) correspond to the approximate formula in Eq. (10). Parameters are the same as in Fig. 3.

parameters considered, $\psi_{n\pm}(t)$ are approximately Gaussians moving at constant group velocities, $v_{\pm} = \varepsilon'_{p\pm}$, where $\varepsilon'_{p\pm} \equiv (d_k \varepsilon_{k\pm})|_{k=p}$ [see Fig. 2(c)]. The teal lines in Fig. 3(b,c) correspond to the trajectories of the two wave packets. The velocities difference results in the splitting of $P_n(t)$ into two parts.

Figure 3(d-i) shows snapshots of the emitters' population distribution for $p = 0.5$ and $p = 1$ (close to resonance). For $p = 0.5$, the splitting is most pronounced, as the difference $v_+ - v_-$ is maximized as shown in Fig. 2(c). In contrast, close to resonance, $v_+ \approx v_-$ minimizing the splitting on the considered time scale. Instead, ψ_{n+} and ψ_{n-} interfere, resulting in irregular probability density as seen in Fig. 3(g-i).

A. Exciton population dynamics

To explain the fringes in the matter population distributions in Fig. 3(a-c), consider the population of matter's k -th mode,

$$P_k(t) = P_k(0) - P_k(0) \frac{2g^2}{\Delta_k^2} [1 - \cos(\Delta_k t)], \quad (9)$$

where $P_k(0)$ is the initial k -space probability density in Eq. (8). Figure 4 shows the total excitonic population,

$$P_{ex}(t) = \int_{-\pi}^{\pi} P_k(t) dk \approx 1 - \frac{2g^2}{\Delta_p^2} + \frac{2g^2}{\Delta_p^2} \exp\left[-\frac{(\Delta'_p)^2 t^2}{4w^2}\right] \cos(\Delta_p t), \quad (10)$$

where $\Delta'_p \equiv (d_k \Delta_k)|_{k=p}$ [see Fig. 2(b)]. The approximate solution was obtained by first-order expansion of

Δ_k around $k = p$ and it is valid for $w \gg 1$ [see the dashed curves in Fig. 4(d-f)].

The approximate formula shows that $P_{ex}(t)$ oscillates (central) frequency Δ_p , and the bright fringes in Fig. 3(a-c) appear at the local maxima of $P_{ex}(t)$. The oscillations decay due to the Rabi frequency dispersion within the initial wave packet. This decay is described by a Gaussian envelope with a standard deviation $\propto w/|\Delta'_p|$. In our examples, the fastest decay occurs for $p = 0.5$, as the slope of Δ_k is steeper at $k = p = 0.5$ compared to the slope around the local extrema at $k = p = 0, 1$, where the derivative is close to zero [Fig. 2(b)]. The steady-state population, $P_{ex}(t \rightarrow \infty) \approx 1 - 2g^2/\Delta_p^2$, is also determined by the VRS.

B. Moments of the matter population distribution

We consider the first two moments of the emitters' population distribution to quantify the wave packet dynamics. In the continuum limit, sums are approximated by integrals, and the moments are given by (App. C)

$$\langle n(t) \rangle = \int x \rho_{x,x}(t) dx = -i \int \frac{\partial \rho_{k,k+q}^e}{\partial q} \Big|_{q=0} dk, \quad (11)$$

$$\langle n^2(t) \rangle = \int x^2 \rho_{x,x}(t) dx = - \int \frac{\partial^2 \rho_{k,k+q}^e}{\partial q^2} \Big|_{q=0} dk, \quad (12)$$

where $\rho_{x,x}$ is the diagonal elements of the continuous density matrix (i.e., the population of the emitter at position x), $\rho_{k,k+q}^e$ is the element of the continuous k -space density matrix.

The explicit formulas for $\langle n \rangle$ and $\langle n^2 \rangle$ are derived by expressing $\rho_{k,k+q}^e$ in terms of the polaritonic states. Omitting the oscillating contributions stemming from the interference between ψ_{n+} and ψ_{n-} (and the constant $\overline{\langle n^2(0) \rangle} = w^2/2$), we obtain (App. C)

$$\overline{\langle n \rangle} = t \int_{-\pi}^{\pi} P_k(0) [\varepsilon'_{k+} \cos^4(\theta_k) + \varepsilon'_{k-} \sin^4(\theta_k)] dk, \quad (13)$$

$$\overline{\langle n^2 \rangle} = t^2 \int_{-\pi}^{\pi} P_k(0) [[\varepsilon'_{k+}]^2 \cos^4(\theta_k) + [\varepsilon'_{k-}]^2 \sin^4(\theta_k)] dk. \quad (14)$$

Since the excitation is shared between the emitters and cavity modes, $\langle n \rangle$ and $\langle n^2 \rangle$ require normalization by the total excitonic population (i.e., total emitters population)

$$\overline{P_{ex}} = \int_{-\pi}^{\pi} P_k(0) [\cos^4(\theta_k) + \sin^4(\theta_k)] dk. \quad (15)$$

According to Eqs. (13) and (14), for sufficiently narrow $P_k(0)$, the first two moments of the matter distribution are approximately proportional to the weighted average of the group velocities, $v_{\pm} = \varepsilon'_{p\pm}$, and their squares, respectively.

Figure 5(a) shows $\langle n \rangle / P_{ex}$ for several values of initial momentum, p . The marked lines correspond to $\overline{\langle n \rangle} / \overline{P_{ex}}$.

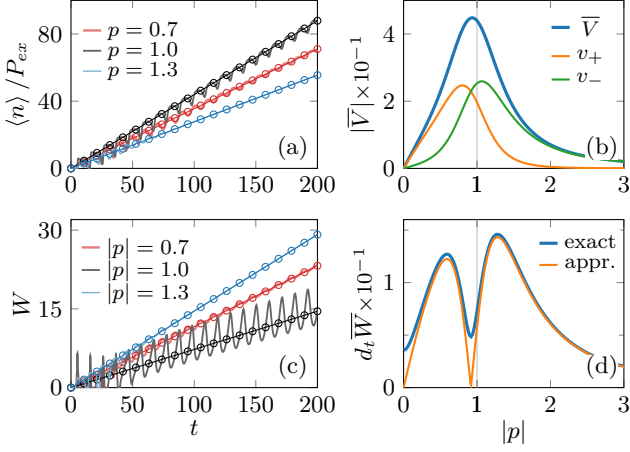


FIG. 5. (a) Normalized CM position, marks correspond to $\langle n \rangle / P_{ex}$ [Eqs. (13) and (15)]. (b) CM velocity, $\bar{V} \equiv d_t [\langle n \rangle / P_{ex}]$. (c) Standard deviation of the emitters' population distribution in Eq. (16), with (solid) and the without (marks) oscillations. (d) The exact and approximate slopes of \bar{W} (see App. B). The parameters are the same as in Fig. 3.

The velocity $\bar{V} = d_t [\langle n \rangle / P_{ex}]$ shown in Fig. 5(b) is a non-monotonous function of initial momentum and peaks at resonance ($p \approx \pm \omega_{eg}$). At this point, v_+ approximately equals v_- , and their weighted sum is maximum.

Next, we consider the standard deviation of the emitters' probability distribution, define as

$$W(t) = \sqrt{\frac{\langle n^2(t) \rangle}{P_{ex}(t)} - \frac{\langle n(t) \rangle^2}{P_{ex}^2(t)} - \frac{w^2}{2}}. \quad (16)$$

Figure 5(c) shows W for several values of p . In contrast to the CM, the wave packet spreading rate is *minimized* at resonance $|p| \approx \omega_{eg}$. Figure 5(d) shows the slope of \bar{W} (W excluding the oscillations), $d_t \bar{W}$. The local minimum at $|p| \approx \omega_{eg}$ can be explained as follows. Two factors contribute to the overall spreading – the spreading of the Gaussians, $\psi_{n\pm}$ relative to their respective centers of mass and the separation of the centers of mass. The approximate $d_t \bar{W}$ presented in Fig. 5(d), includes only the second contribution and captures the local minimum (see App. B). This shows that the rate of distribution spreading is minimized when $\psi_{n\pm}$ move at the same group velocity, i.e., when $v_- = v_+$. The wave packet exhibits a soliton-like behavior at resonance.

IV. DYNAMICS IN PRESENCE OF STOCHASTIC NOISE ACTING ON EMITTERS

This section analyzes the emitter's probability distribution in the stochastic multi-mode TC model framework. Adopting the Haken-Strobl-Reineker (HSR) model to describe the noise [52], the transition energy of

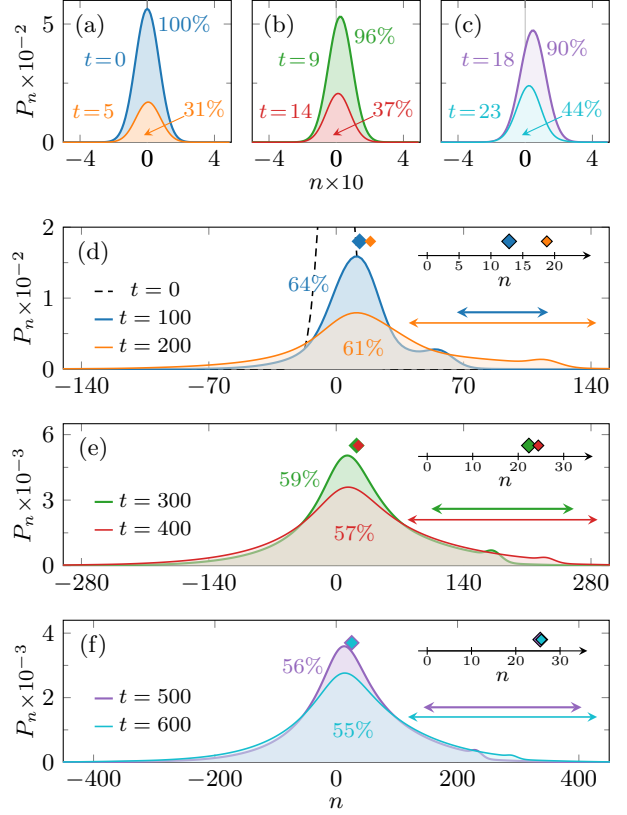


FIG. 6. (a-c) Rabi oscillations on the short time scale. (d-f) P_n at later times. Diamonds denote the CM position, and the double-headed arrows represent the width of P_n (proportional to standard deviation). The instantaneous total excitonic population is given as a percentage. Parameters: $\rho = 1$, $\omega_c = 0.4$, $g = 0.3$, $\Gamma = 0.03$, $p = 0.5$, $w = 10$.

each emitter receives an independent stochastic contribution, $\xi_n(t)$, with auto-correlation function $\xi_m(t)\xi_n(t') = \Gamma \delta_{m,n} \delta(t - t')$, where $\Gamma = \tilde{\Gamma}/\omega_{eg}$ is the dimensionless dephasing rate, proportional to temperature. The HSR model allows for analytic averaging over the noise, resulting in the master equation for the $2N \times 2N$ density matrix of the exciton-photon system

$$\frac{\partial \hat{\rho}}{\partial t} = -i[\hat{H}, \hat{\rho}] - \frac{\Gamma}{2} \sum_{n=1}^N [[b_n] \langle b_n |, [[b_n] \langle b_n |, \hat{\rho}]]. \quad (17)$$

The terms proportional to Γ destroy the coherences within the excitonic quadrant of the density matrix (off-diagonal elements within the quadrant), as well as the light-matter coherences (all elements of the off-diagonal quadrants of the density matrix).

In the presence of noise, the dynamics are no longer invariant with respect to the number density, ρ , in contrast to the noise-free case in Sec. III. As we discuss later, noise homogenizes the initial k -space distribution, and the scaling of the initial state variables becomes irrelevant on the long-time scale. Thus, in this section, we fix the system parameters: $\omega_{eg} = 2.1$ eV, $\ell = 0.590 \mu\text{m}$,

$L = 590\mu\text{m}$. The number of photonic modes equals the number of emitters, $N = 1001$, such that $\rho = 1$.

Figure 6 shows snapshots of emitters' probability distributions in the presence of noise, obtained by direct numerical solution of Eq. (17). The figure suggests that the wave packet evolves through a sequence of qualitatively different dynamical stages across several time scales. On the short time scale presented in Fig. 6(a-c), the CM and the wave packet width remain almost unchanged, while the the distribution's peak oscillates due to the coherent population exchange between the light and matter subsystems (Rabi oscillations, Subsec. III A). After the initial phase of rapid exchange, the population relaxes slowly. Relaxation lasts until an equal population partition between the subsystems is reached.

While the initial wave packet CM velocity is the same as in Fig. 5(b), due to noise, it slows down and stops after $t \approx 200$. See the sequence of diamonds representing the CM position in panels (d-f). In contrast, the wave packet width, represented by the double-headed arrows, continues to increase after the CM stops. Thus, the stages of the matter wave packet evolution are (from the shortest to longest): (a) Rabi oscillations, (b) damping of CM motion, (c) population relaxation, (d) transition from ballistic to diffusive spreading.

For further analysis, we utilize the spatial invariance of the emitters' lattice and rewrite the master equation in terms of the Bloch states. This results in a reduced set of equations for the k -space density matrix elements

$$\dot{\rho}_{k,k+q}^e = -2ig\text{Im}[\rho_{k,k+q}^{p-e}] - \Gamma\rho_{k,k+q}^e + \frac{\Gamma}{N} \sum_p \rho_{p,p+q}^e, \quad (18a)$$

$$\dot{\rho}_{k,k+q}^p = -i(\omega_k - \omega_{k+q})\rho_{k,k+q}^p - 2ig\text{Im}[\rho_{k,k+q}^{e-p}], \quad (18b)$$

$$\begin{aligned} \dot{\rho}_{k,k+q}^{p-e} &= -i(\omega_k - \omega_{\text{eg}} - i\Gamma/2)\rho_{k,k+q}^{p-e} \\ &\quad - ig(\rho_{k,k+q}^e - \rho_{k,k+q}^p), \end{aligned} \quad (18c)$$

$$\begin{aligned} \dot{\rho}_{k,k+q}^{e-p} &= -i(\omega_{\text{eg}} - \omega_{k+q} - i\Gamma/2)\rho_{k,k+q}^{e-p} \\ &\quad - ig(\rho_{k,k+q}^p - \rho_{k,k+q}^e), \end{aligned} \quad (18d)$$

where $\rho_{k,k+q}^e$ is an element in the first quadrant (excitonic quadrant), $\rho_{k,k+q}^p$ is an element in the fourth quadrant (cavity or photonic quadrant), and $\rho_{k,k+q}^{p-e}$, $\rho_{k,k+q}^{e-p}$ are elements in the second and third, i.e., off-diagonal quadrants of the density matrix. Setting $q = 0$ shows that the populations of k -th exciton and k -th cavity modes are coupled through light-matter coherence. Fig. 7 illustrates the k -space density matrix and shows some of its elements with $q = 0$.

The effect of noise is two-fold. First, it damps the light-matter coherences at rate $\Gamma/2$. Secondly, the last two terms in Eq. (18a) tend to *homogenize* the population among the exciton modes. Figure 8 shows snapshots of excitonic (P_k^e) and photonic (P_k^p) distributions. On the short time scale, the distributions remain at the initial positions defined by the initial momentum, p , and oscillate due to the exchange of the population between the light and matter subsystems (Rabi oscillations). With

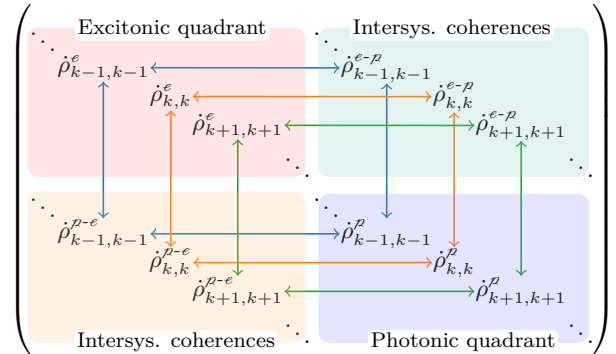


FIG. 7. Illustration of the k -space density matrix. Diagonal elements within the four quadrants (elements with $q = 0$) and the couplings between them are shown.

time, due to the noise-induced homogenization, baselines are built in the excitonic distributions. Simultaneously, all photonic modes become gradually populated. Later, at $t \approx 100 - 200$, the excitonic distribution becomes *symmetric* relative to $k = 0$, which explains the termination of CM motion, as the average momentum vanishes [see Fig. 6(e,f)]. The population relaxation continues until both P_k^e and P_k^p become uniform.

A. Population relaxation: thermalization process

Figure 9(a,b) shows the evolution of the total excitonic population in the presence of noise. In contrast to the isolated system in Fig. 4, the Rabi oscillations here decay on a time scale of $2/\Gamma$, regardless of the initial momentum p . The population slowly relaxes towards the equilibrium value of $1/2$ on the longer time scale. This behavior is expected as the thermalization is independent of the initial state. The relaxation time scales can be roughly estimated by neglecting the homogenizing terms in Eq. (18a), which may be justified when the excitonic population distribution is approximately uniform. Then, the system reduces to a collection of independent TLS where only the k -th exciton is coupled to stochastic noise. Population dynamics in such TLS has an oscillating contribution that decays at a rate $\sim \Gamma/2$, and decaying at rate s_k contribution, where (see App. D for details)

$$s_k \approx \frac{2g^2\Gamma}{4g^2 + \delta_k^2}, \quad \delta_k = \omega_k - \omega_{\text{eg}}. \quad (19)$$

With the homogenizing terms, all the matter modes become populated with time. The detuning of most modes from the corresponding cavity modes gives rise to the slow relaxation seen in Fig. 9(a,b).

For quantitative time scale analysis, we consider the eigenvectors and eigenvalues of the $4N \times 4N$ non-Hermitian matrix defining the linear system in Eq. (18). The total exciton population can be expressed as $P_{\text{ex}} = \sum_{n=1}^{4N} c_n \exp(\lambda_n t)$, where λ_n are the eigenvalues,

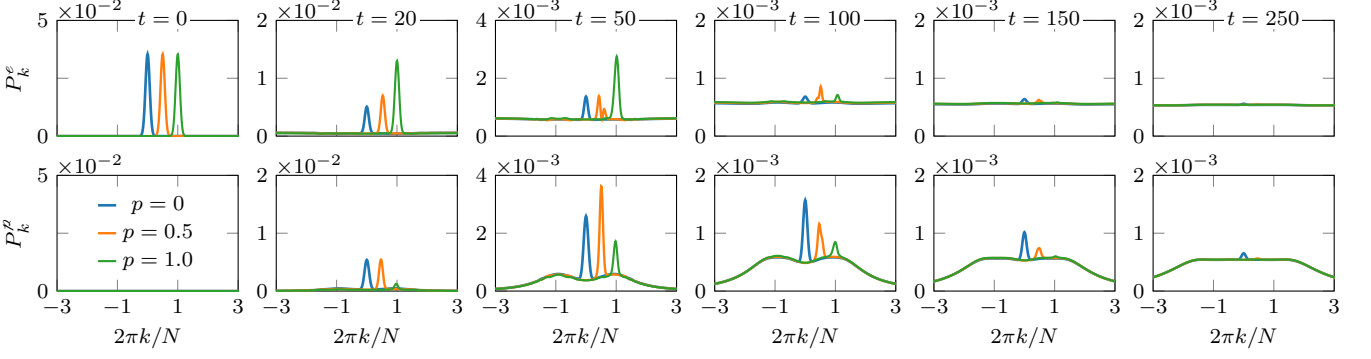


FIG. 8. Snapshots of exciton (top row) and cavity modes (bottom row) population distributions at selected times. With time, the excitonic population distribution becomes symmetric relative to $k = 0$. This is when the CM stops. Parameters: $\rho = 1$, $\omega_c = 0.4$, $g = 0.3$, $\Gamma = 0.1$, $w = 10$.

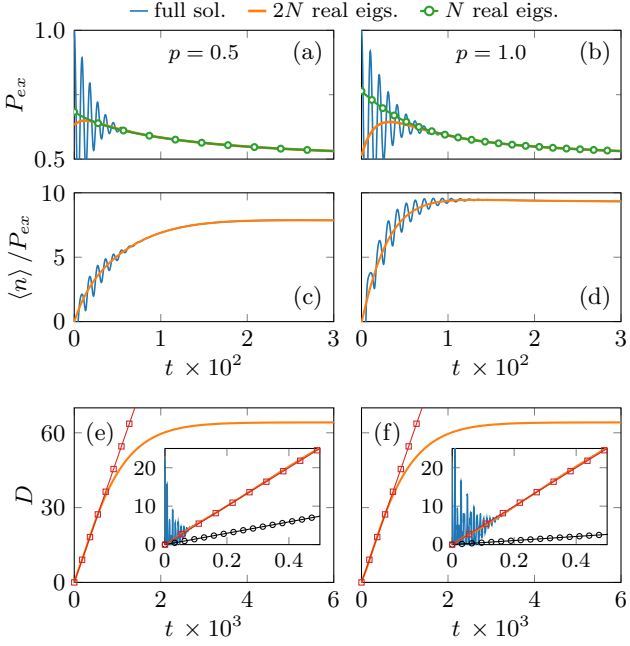


FIG. 9. (a,b) Total excitonic population. (c,d) Position of the matter wave packet CM. (e,f) Diffusivity of the matter wave packet. Circles correspond to the noise-free cases. The squares approximate D in the ballistic regime using the model $[a(1 - e^{-1}) - b/e]t$ in Eq. (27). The slope value is 0.05, independent of Γ and p . Parameters: $\rho = 1$, $\omega_c = 0.4$, $g = 0.3$, $w = 10$, $\Gamma = 0.1$.

and c_n depend on the eigenvectors and the initial state, and can be found by Moore–Penrose pseudo-inverse. Figure 10(a,b) shows an example set of eigenvalues, λ_n . All the eigenvalues with non-zero imaginary parts have nearly constant real parts, $-\Gamma/2$. This implies that the oscillations decay at a rate of $\Gamma/2$ as seen in Fig. 9(a,b). Considering only the real eigenvalues (with zero imaginary part) results in the smooth orange curves.

To determine the relaxation time scale, we focus on the N smallest real-valued eigenvalues ($-\Gamma/2 < \lambda_n \leq 0$). Only those eigenvalues contribute to the marked green curves in Fig. 9(a,b). We found numerically that these eigenvalues have linear scaling with Γ (for $\Gamma \leq 0.3$) (see App. E).

Processes described by a sum of decaying exponentials are encountered e.g., in studies of time-resolved luminescence spectroscopy of molecular, macromolecular, supramolecular, and nanosystems [53]. A stretched exponential (Kohlrausch) function is often used to model and quantify such processes. Excellent fits are obtained using the model $a \exp(-\alpha t^\beta) + 1/2$, and β is found to be close to $2/3$ (see App. F).

For simplicity and physical clarity, however, here we estimate the effective decay rate of the population, λ_{eff}^P by

$$[\lambda_{eff}^P]^{-1} = \frac{\int_0^\infty t[f(t) - 1/2] dt}{\int_0^\infty [f(t) - 1/2] dt}, \quad (20)$$

where $f(t)$ is the population signal. When $f(t)$ taken to be the smoothed out signal, λ_{eff}^P is proportional to Γ as shown in Fig. 10(c). This is consistent with the linear Γ dependence of the smallest real-valued eigenvalues. When $f(t)$ is taken to be the full signal including the oscillations, $\lambda_{eff}^P(\Gamma)$ shows slight deviation from the linear Γ -dependence (see App. G). These findings suggest that population relaxation is slower than Rabi oscillation decay. Averages of $N/2$ smallest eigenvalues and averages of the corresponding TLS rates, s_k are comparable and can be used as rough estimates of λ_{eff}^P (see App. E). Figure 10(d) shows that λ_{eff}^P has a relatively weak dependence on the initial momentum p .

B. CM motion of the matter distribution

Figure 9(c,d) shows two examples of matter distribution CM dynamics. Appendix H outlines our approach

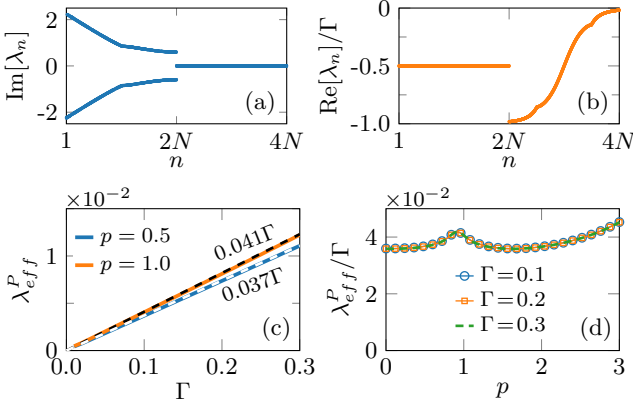


FIG. 10. (a,b) Eigenvalues of the linear system in Eq. (18). Here, $q = 0$, $\Gamma = 0.1$. (c,d) Effective relaxation rate of the total excitonic population, P_{ex} , see Eq. (20). Note that in (d), λ_{eff}^P is scaled by Γ . Parameters: $\rho = 1$, $\omega_c = 0.4$, $g = 0.3$, $w = 10$.

to evaluating $\langle n(t) \rangle$ using Eq. (18). The smooth orange curves were obtained by including only the real-valued eigenvalues. The noise slows down and eventually stops the CM motion. Qualitatively, this is similar to propagation on a simple 1D quantum lattice (without the cavity). In that case, the CM position is given by [25]

$$\langle n \rangle = \frac{1 - e^{-\Gamma t}}{\Gamma} \int_{-\pi}^{\pi} \varepsilon'_k P_k(0) dk, \quad (21)$$

where $\varepsilon'_k \equiv d_k(\varepsilon_k)$, and ε_k is the lattice dispersion relation. The formula shows that the asymptotic position is proportional to Γ^{-1} for a fixed initial momentum. For comparison, Fig. 11(a,b) shows the asymptotic values of the CM

$$\langle n \rangle_{asy} \equiv \frac{\langle n(t \rightarrow \infty) \rangle}{P(t \rightarrow \infty)} = 2 \langle n(t \rightarrow \infty) \rangle, \quad (22)$$

where we used the fact that $P(t \rightarrow \infty) = 1/2$. The k -space periodicity is reflected in the periodicity of $\langle n \rangle_{asy}$ plotted as a function of p .

Despite the similarities with the simple lattice case outside a cavity, cavity system exhibits very different behavior quantitatively. The CM velocity decay rate here is *significantly lower* than Γ . To estimate this rate, we use

$$[\lambda_{eff}^V]^{-1} = \frac{\int_0^\infty t |f(t)| dt}{\int_0^\infty |f(t)| dt}, \quad (23)$$

where $f(t)$ is the velocity derived from the smooth orange curves in Fig. 9(c,d). Figure 11(c,d) shows λ_{eff}^V as a function of Γ and p . Close to resonance ($p \approx \omega_{eg}$), the decay rate of the CM velocity is an order of magnitude larger than the population relaxation.

Qualitatively, the difference in population relaxation and CM velocity decay rates can be seen through the

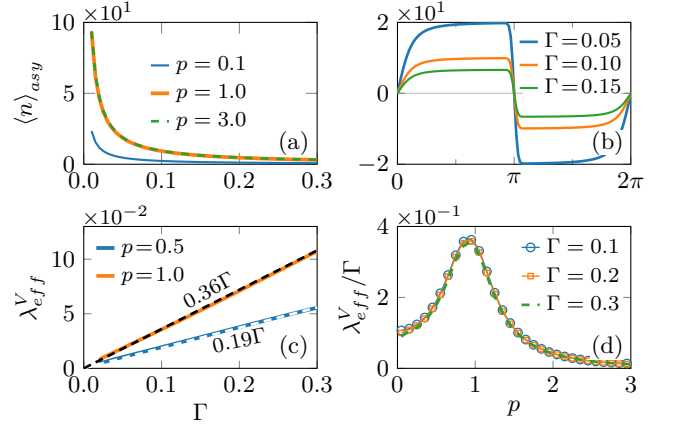


FIG. 11. Asymptotic position of the matter CM distribution as a function of Γ (a), and initial momentum, p (b). The periodicity in (b) stems from the k -space periodicity. (c,d) Effective decay rate of the CM velocity in Eq. (23). Parameters: $\rho = 1$, $\omega_c = 0.4$, $g = 0.3$, $w = 10$.

evolution of matter and cavity modes population distributions. Figure 8 shows that by the time $t \approx 150$ the excitonic distribution becomes nearly symmetric and uniform. The symmetry implies vanishing average momentum, which is consistent with Fig. 9(c,d) where the CM indeed stops after $t \approx 200$. In contrast, the cavity distribution is not yet homogeneous, and the population exchange between the subsystems continues.

C. Diffusivity: ballistic-diffusive transition

Next, we consider the rate of the matter distribution spreading, i.e., the diffusivity [compare with Eq. (16)]

$$2D(t) \equiv \frac{d}{dt} \left[\frac{\langle n(t)^2 \rangle}{P_{ex}(t)} - \frac{\langle n(t) \rangle^2}{P_{ex}^2(t)} \right]. \quad (24)$$

Appendix H outlines our approach to evaluating $\langle n^2(t) \rangle$ using Eqs. (18). Figure 9(e,f) shows two examples of the time-dependent diffusivity that undergoes a transition from ballistic ($D \propto t$) to diffusive ($D \approx \text{const.}$) behavior. The transition is associated with noise-induced dephasing and the homogenizing terms in Eq. (18a).

In the case of 1D quantum lattice with HSR noise, the diffusivity of a wave packet with stationary CM is given by

$$D(t) = C_1 \frac{1 - e^{-\Gamma t}}{\Gamma} + C_2 e^{-\Gamma t} t, \quad (25a)$$

$$C_1 = \int_{-\pi}^{\pi} \frac{(\varepsilon'_k)^2}{2\pi} dk, \quad (25b)$$

$$C_2 = \int_{-\pi}^{\pi} (\varepsilon'_k)^2 \left[P_k(0) - \frac{1}{2\pi} \right] dk. \quad (25c)$$

Figure 12(a) presents the diffusion constant, $D_{asy} \equiv D(t \rightarrow \infty) \approx a/\lambda_{eff}^D$. For the considered values of Γ ($0.01 \leq \Gamma \leq 0.3$), D_{asy} scales as Γ^{-1} independent of the initial state. For comparison, the diffusion constant in a 1D lattice with nearest-neighbor coupling, J is given by $D_{lattice}(t \rightarrow \infty) = 2J^2/\Gamma$.

To study the diffusivity time dependence, we use the model suggested by Eq. (25a)

$$f(t) = a \frac{1 - e^{-\lambda_{eff}^D t}}{\lambda_{eff}^D} - b e^{-\lambda_{eff}^D t}. \quad (26)$$

This model has three free parameters: a , b , and λ_{eff}^D , and provides excellent fits for the system parameters considered. Figure 12(b) shows λ_{eff}^D as a function of Γ . While the ballistic-diffusion transition rate in the lattice is Γ^{-1} , the rate here is significantly slower, $\lambda_{eff}^D = 0.02\Gamma$. Like the lattice without a cavity, the rate is independent of the initial momentum.

Importantly, the transient diffusivity in the ballistic regime is significantly enhanced compared to the diffusivity in the isolated system. Figure 9(e,f) compares the diffusivity in the isolated system (black circles) vs the linear approximation denoted by red squares,

$$\lambda_{eff}^D f(1/\lambda_{eff}^D t) = [a(1 - e^{-1}) - b/e]t. \quad (27)$$

The slope, $a(1 - e^{-1}) - b/e \approx 0.05$ (for $\rho = 1$, $\omega_c = 0.4$, $g = 0.3$) is independent of p and Γ for the considered values of $\Gamma \geq 0.02$. Noise-induced transient diffusivity enhancement has been studied in quantum lattices without the cavity [25]. In our multimode cavity system, the duration of the enhanced expansion is significantly extended due to the slow ballistic-diffusion transition rate. Figure 12(c) compares the approximate slope of $D(t)$ in the ballistic regime, $a(1 - e^{-1}) - b/e$ vs the slopes in the isolated system (dashed curve). We added the initial slope of $D(t)$ and $(a - b)$ for comparison.

V. SUMMARY, EXPERIMENTAL REALIZATION, AND OUTLOOK

The presented theoretical analysis characterizes the essential features of polariton wave packet dynamics in an effectively 1D multi-mode microcavity with or without noise acting on the emitters.

The two polariton branches give rise to the emitters' population distribution splitting in the absence of noise. The wave function of the matter subsystem is a superposition of two Gaussians moving with different group velocities defined by the derivatives of the polariton energies. The weighted averages of these group velocities determine the first two moments of the emitters' distribution, which define the CM position and diffusivity (the rate of distribution spreading). The two moments are non-linear functions of the initial momentum. At resonance, the CM velocity reaches its maximum while the

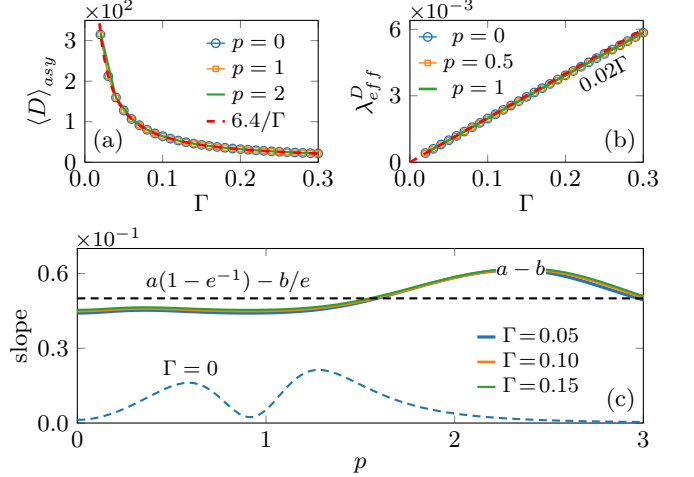


FIG. 12. (a) Diffusion constant. (b) Effective ballistic-diffusive transition rate. (c) Approximate slope of $D(t)$ in the presence of noise during the ballistic stage, $a(1 - e^{-1}) - b/e$, $(a - b)$ [see Eqs. (26) and (27)] vs. the slope in the isolated system ($\Gamma = 0$). Parameters: $\rho = 1$, $\omega_c = 0.4$, $g = 0.3$, $w = 10$.

spreading rate is minimized, suggesting *soliton-like* behavior.

Noise acting on the emitters induces dephasing in the system. It causes significant changes in the dynamics of the emitter's population distribution, which proceeds through a sequence of stages across vastly different time scales. These stages include Rabi oscillations, CM velocity damping, population relaxation, and the transition from the ballistic to the diffusive regime of distribution expansion. The time scales of these stages establish a universal hierarchy, $\Gamma^{-1} < (\lambda_{eff}^V)^{-1} < (\lambda_{eff}^P)^{-1} < (\lambda_{eff}^D)^{-1}$. Here, Γ is the white noise's intensity. The initial stage, characterized by the rapid decay of Rabi oscillations, occurs on the time scale of Γ^{-1} . λ_{eff}^V is the rate of CM velocity damping, λ_{eff}^P is the population relaxation rate, and λ_{eff}^D is the rate of ballistic-diffusive transition. Notably, λ_{eff}^V , λ_{eff}^P , and λ_{eff}^D can be smaller than Γ by several orders of magnitude. This contrasts sharply with wave packet dynamics in simpler 1D lattices without cavities (including direct inter-emitter interactions) where all time-dependent observables have a single characteristic time scale, Γ^{-1} .

Another striking effect in the presence of noise is that the initial ballistic expansion persists for several orders of magnitude longer than the dephasing time in a lattice without the cavity. Moreover, the rate of expansion is substantially enhanced by noise compared to the noise-free case.

Note that the model adopted here is a generalization of the HSR model, which assumes a classical stochastic noise, to a multimode cavity system [54, 55]. In other models, emitters' vibrational degrees of freedom are often treated classically or semi-classically [47, 56].

Such approaches may not fully capture the system coherences and become less reliable at low temperatures or under strong vibronic coupling [57]. Coherences may also affect the thermalization process [50, 58, 59]. Thus, our model is more reliable during the ballistic expansion stage before thermalization and qualitatively captures the diffusive transport after thermalization. These reservations also apply to other semi-classical simulations attempting to describe post-thermalization diffusion.

Experimental realization.— Polariton dispersion curves and the corresponding group velocities are often used for interpreting experimental results focusing on the first two moments of the population distribution in the matter subsystem [36–39]. However, microscopy measurements tracking the spatiotemporal profile of the wave packet provide information beyond the first two moments. In line with our analysis, recent experiments have shown evidence of distribution splitting [36]. Moreover, on sufficiently short timescales, before the effects of disorder or dephasing manifest, the predictions in noise-free case (Sec. III), such as the dependence on initial momentum, can, in principle, be tested experimentally.

Ballistic expansion at a fraction of the speed of light is expected in a noise-free and disorder-free polariton system. Remarkably, recent experiments demonstrated ballistic expansion, *despite* the disorder and dissipative effects [15, 33, 36–39, 60]. Our theoretical results are consistent with these experiments and predict noise-enhanced ballistic expansion persisting on timescales several orders of magnitude longer than the dephasing time without a cavity. The noise intensity Γ is proportional to temperature, and all the time scales related to dynamical observables were shown to be proportional to Γ^{-1} . Both temperature and the initial state can be controlled, making our theoretical predictions amenable to experimental verification. However, long observation times may be necessary to confirm the predicted extended ballistic spreading and the slow transition to a diffusive regime.

Outlook.— Inter-emitter interactions (such as Förster-like energy transfer [10, 61]), cavity losses, static disorder, and other physical processes may further influence ballistic expansion of the emitters' probability distribution. The effective master equation developed here allows for the straightforward inclusion of some of those, particularly inter-emitter interactions and cavity loss, paving the way for a more detailed description of specific experimental conditions. A comprehensive description of realistic emitters, like molecules, requires accounting for the vibrational degrees of freedom (i.e., vibronic coupling). Future work will analyze systems that include vibronic coupling and other complexities mentioned above.

Appendix A: Transformation from sites basis to exciton basis

This Appendix shows the steps leading to the Hamiltonian in Eq. (4).

The Hamiltonian in Eq. (2) can be simplified by using the exciton states, $|b_j\rangle$ as the basis for the emitters' subsystem. $|b_j\rangle$'s are defined as

$$|b_j\rangle = \frac{1}{\sqrt{N}} \sum_{n=1}^N e^{i \frac{2\pi}{N} j n} |b_n\rangle, \quad |b_n\rangle = \frac{1}{\sqrt{N}} \sum_j e^{i \frac{2\pi}{N} j n} |b_j\rangle. \quad (\text{A1})$$

Substitution into the first coupling term in the Hamiltonian yields

$$\begin{aligned} & \frac{\tilde{g}}{\sqrt{LN}} \sum_{j,k,n} e^{i \frac{2\pi}{N} k n} e^{-i \frac{2\pi}{N} j n} |a_k\rangle \langle b_j| \\ &= \tilde{g} \sqrt{\frac{N}{L}} \sum_{j,k} \underbrace{\left[\frac{1}{N} \sum_n e^{i \frac{2\pi}{N} (k-j)n} \right]}_{=\delta_{kj}} |a_k\rangle \langle b_j| \\ &= \tilde{g} \sqrt{\frac{N}{L}} \sum_{k=-N/2}^{k=N/2} |a_k\rangle \langle b_k|. \end{aligned} \quad (\text{A2})$$

The second coupling term (complex conjugate of the first one) is treated similarly. The second term of Eq. (2) keeps its form in the new basis. Thus, the basis transformation results in the Hamiltonian in Eq. (4).

Appendix B: Emitters' wave function

This Appendix outlines the derivation of the matter wave function in the isolated system.

First, we find the expansion coefficients of the initial state in terms of the polaritons,

$$\begin{aligned} c_{k\pm} &= \langle v_{k\pm} | \psi_n(0) \rangle = \begin{cases} \cos(\theta_k) \langle b_k | \psi_n(0) \rangle, & +, \\ \sin(\theta_k) \langle b_k | \psi_n(0) \rangle, & -, \end{cases} \\ &= \begin{cases} \cos(\theta_k) \frac{\sqrt{w}}{\pi^{1/4}} e^{-w^2(k-p)^2/2}, & +, \\ \sin(\theta_k) \frac{\sqrt{w}}{\pi^{1/4}} e^{-w^2(k-p)^2/2}, & -, \end{cases} \end{aligned} \quad (\text{B1})$$

where we used the k -space representation of the initial state in Eq. (8). The time-dependent wave function in the polariton basis is given by

$$\begin{aligned} \psi(t) &= \sum_k \cos(\theta_k) \frac{\sqrt{w} e^{-w^2(k-p)^2/2}}{\pi^{1/4}} e^{-i\varepsilon_{k+}t} |v_{k+}\rangle \\ &+ \sum_k \sin(\theta_k) \frac{\sqrt{w} e^{-w^2(k-p)^2/2}}{\pi^{1/4}} e^{-i\varepsilon_{k-}t} |v_{k-}\rangle. \end{aligned} \quad (\text{B2})$$

where $\varepsilon_{k\pm}$ is the polariton energy given by Eq. (6a).

Next, to find the emitters' wave function, $\psi_n(t)$, the wave function is projected onto the emitter site basis,

$|b_n\rangle$. The wave function is given as a sum of two wave packets formed with upper and lower polaritons, $\psi_n(t) = \psi_{n+}(t) + \psi_{n-}(t)$, where

$$\psi_{n+} = \frac{1}{\pi\sqrt{2}} \int_{-\pi}^{\pi} \cos^2(\theta_k) e^{-\frac{w^2}{2}(k-p)^2} e^{-i\varepsilon_{k+}t+ikn} dk, \quad (\text{B3a})$$

$$\psi_{n-} = \frac{1}{\pi\sqrt{2}} \int_{-\pi}^{\pi} \sin^2(\theta_k) e^{-\frac{w^2}{2}(k-p)^2} e^{-i\varepsilon_{k-}t+ikn} dk. \quad (\text{B3b})$$

Figure 3 shows the emitters' probability density splitting into two parts due to the difference in the phase velocities between ψ_{n+} and ψ_{n-} . By dropping the interference terms, the population distribution can be approximated by $P_n(t) = |\psi_n(t)|^2 \approx |\psi_{n+}|^2 + |\psi_{n-}|^2$.

To evaluate the integrals in Eqs. (B3a) and (B3b), we expand $\varepsilon_{k\pm}$ about $k = p$ up to the second order in k . For sufficiently wide in real space initial states ($w \gg 1$, i.e., narrow in k space), $\cos^2(\theta_k)$ and $\sin^2(\theta_k)$ in the integral can be approximated by $\cos^2(\theta_p)$ and $\sin^2(\theta_p)$. This yields

$$|\psi_{n\pm}|^2 \approx \begin{cases} \frac{\cos^4(\theta_p)}{\sqrt{2\pi\sigma^2}} e^{-\frac{(x-v_{\pm}t)^2}{2\sigma_{\pm}^2(t)}}, & +, \\ \frac{\sin^4(\theta_p)}{\sqrt{2\pi\sigma^2}} e^{-\frac{(x-v_{\pm}t)^2}{2\sigma_{\pm}^2(t)}}, & - \end{cases} \quad (\text{B4})$$

where

$$v_{\pm} = \varepsilon'_{p\pm}, \quad \sigma_{\pm}^2(t) = \frac{w^2}{2} + \frac{[\varepsilon''_{p\pm}]^2}{2w^2} t^2. \quad (\text{B5})$$

are the group velocities and variances associated with $\psi_{n\pm}$. In this approximation, the standard deviation of the matter distribution is given by

$$\begin{aligned} (d_t \bar{W})^2 &= \frac{\cos^4(\theta_p)v_+^2 + \sin^4(\theta_p)v_-^2}{\cos^4(\theta_p) + \sin^4(\theta_p)} \\ &+ \frac{2}{w^2} \frac{\cos^4(\theta_p)[\varepsilon''_{p+}]^2 + \sin^4(\theta_p)[\varepsilon''_{p-}]^2}{\cos^4(\theta_p) + \sin^4(\theta_p)} \\ &- \left[\frac{\cos^4(\theta_p)v_+ + \sin^4(\theta_p)v_-}{\cos^4(\theta_p) + \sin^4(\theta_p)} \right]^2. \end{aligned} \quad (\text{B6})$$

For consistency with the assumption $w \gg 1$, we neglect the spreading relative to the centers of mass of the constituent wave packets, which yields a simplified formula

$$\begin{aligned} (d_t \bar{W})^2 &\approx \frac{\cos^4(\theta_p)v_+^2 + \sin^4(\theta_p)v_-^2}{\cos^4(\theta_p) + \sin^4(\theta_p)} \\ &- \left[\frac{\cos^4(\theta_p)v_+ + \sin^4(\theta_p)v_-}{\cos^4(\theta_p) + \sin^4(\theta_p)} \right]^2. \end{aligned} \quad (\text{B7})$$

Figure 5(d) compares the numerically exact $d_t \bar{W}$ and the approximation in Eq. (B7). The agreement between the two results suggests that the relative motion between the two wave packets determines the spreading of the probability distribution.

Appendix C: Moments of the matter distribution in the isolated system

This Appendix presents the general formulas for the moments of the matter population distribution. Additionally, analytical expressions are derived in the noise-free case.

In the continuum limit, the diagonal element of the real-space matter density matrix (i.e., emitters' populations) in terms of the continuous k -space density matrix reads

$$\begin{aligned} \rho_{x,x} &= \frac{1}{2\pi} \int e^{-ixk} \rho_{k,k}^e e^{ixk'} dk dk' \\ &= \frac{1}{2\pi} \int e^{-ixk} \rho_{k,k+q}^e e^{ix(k+q)} dk dq. \end{aligned} \quad (\text{C1})$$

Thus, the CM position is given by

$$\begin{aligned} \langle n \rangle &= \frac{1}{2\pi} \int \int \rho_{k,k+q}^e \overbrace{\left[\int x e^{ixq} dx \right]}^{\propto \delta'(q)} dk dq \\ &= -i \int \frac{\partial \rho_{k,k+q}^e}{\partial q} \Big|_{q=0} dk \equiv -i \int [\rho_{k,k}^e]' dk. \end{aligned} \quad (\text{C2})$$

Similarly, we can obtain the second moment of the emitters' distribution

$$\begin{aligned} \langle n^2 \rangle &= \frac{1}{2\pi} \int \int \rho_{k,k+q}^e \overbrace{\left[\int x^2 e^{ixq} dx \right]}^{\propto \delta''(q)} dk dq \\ &= - \int \frac{\partial^2 \rho_{k,k+q}^e}{\partial q^2} \Big|_{q=0} dk \equiv - \int [\rho_{k,k}^e]'' dk. \end{aligned} \quad (\text{C3})$$

Density matrix of the matter subsystem.—The density matrix of the composite system in terms of polaritons is given by

$$\hat{\rho} = \sum_{p,p'} \rho_{pp'} |v_p\rangle \langle v_{p'}|, \quad (\text{C4})$$

where $|v_p\rangle$ and $|v_{p'}\rangle$ are the polariton states

$$|v_{p\pm}\rangle = \begin{cases} -\sin(\theta) |a_p\rangle + \cos(\theta) |b_p\rangle, & + \\ \cos(\theta) |a_p\rangle + \sin(\theta) |b_p\rangle, & - \end{cases} \quad (\text{C5})$$

The density matrix of the matter subsystem can be obtained by projecting onto the emitters site basis states, $|b_n\rangle$, $\rho_{k,k'}^e = \langle b_k | \hat{\rho} | b_{k'} \rangle = \sum_{p,p'} \rho_{pp'} \langle b_k | v_p \rangle \langle v_{p'} | b_{k'} \rangle$. Explicitly,

$$\begin{aligned} \rho_{k,k+q}^e &= \rho_{k-,k-+q}(t) \sin(\theta_k) \sin(\theta_{k+q}) \\ &+ \rho_{k-,k++q}(t) \sin(\theta_k) \cos(\theta_{k+q}) \\ &+ \rho_{k+,k-+q}(t) \cos(\theta_k) \sin(\theta_{k+q}) \\ &+ \rho_{k+,k++q}(t) \cos(\theta_k) \cos(\theta_{k+q}). \end{aligned} \quad (\text{C6})$$

On the right-hand side appear elements of the density matrix expressed on a polaritonic basis. In the isolated system, these elements are given by:

$$\rho_{k\pm,k\pm+q}(t) = \rho_{k\pm,k\pm+q}(0)e^{-i(\varepsilon_{k\pm}-\varepsilon_{k\pm+q})t}, \quad (\text{C7})$$

where $\varepsilon_{k\pm}$ are the polariton energies [see Eq. (6a)], and $\rho_{k\pm,k\pm+q}(0)$ is defined by the initial state.

1. Exciton population

To find the explicit formula for the total excitonic population (total population in the emitters' subsystem), we must find explicit expressions for the time-dependent density matrix elements expressed in the polaritonic basis appearing in Eq. (C6).

The initial density matrix of the matter subsystem is [Eq. (7)]

$$\rho_{m,n}(0) = \frac{1}{w^2\pi} e^{-\frac{m^2+n^2}{2w^2}+ipm-ipn}. \quad (\text{C8})$$

The cavity modes are assumed to be unpopulated $t = 0$. The density matrix elements in the polaritonic basis are given by

$$\begin{aligned} \rho_{k-,k-}(0) &= \langle v_{k-} | \rho_{m,n} | v_{k-} \rangle \\ &= \sin^2(\theta_k) \sum_{m,n} \rho_{m,n} \langle b_k | m \rangle \langle b_k | n \rangle, \end{aligned} \quad (\text{C9a})$$

$$\begin{aligned} \rho_{k-,k+}(0) &= \langle v_{k-} | \rho_{m,n} | v_{k+} \rangle \\ &= \sin(\theta_k) \cos(\theta_k) \sum_{m,n} \rho_{m,n} \langle b_k | m \rangle \langle b_k | n \rangle, \end{aligned} \quad (\text{C9b})$$

$$\begin{aligned} \rho_{k+,k-}(0) &= \langle v_{k+} | \rho_{m,n} | v_{k-} \rangle \\ &= \sin(\theta_k) \cos(\theta_k) \sum_{m,n} \rho_{m,n} \langle b_k | m \rangle \langle b_k | n \rangle, \end{aligned} \quad (\text{C9c})$$

$$\begin{aligned} \rho_{k+,k+}(0) &= \langle v_{k+} | \rho_{m,n} | v_{k+} \rangle \\ &= \cos^2(\theta_k) \sum_{m,n} \rho_{m,n} \langle b_k | m \rangle \langle b_k | n \rangle. \end{aligned} \quad (\text{C9d})$$

Approximating the sums by integrals results in

$$\begin{aligned} P_k(0) &= \sum_{m,n} \rho_{m,n} \langle b_k | m \rangle \langle b_k | n \rangle \\ &\approx \frac{1}{2\pi} \iint \frac{1}{w\sqrt{\pi}} e^{-\frac{x^2+y^2}{2w^2}+ipx-ipy} e^{-ikx} e^{iky} dx dy \\ &= \frac{w}{\sqrt{\pi}} e^{-w^2(k-p)^2}. \end{aligned} \quad (\text{C10})$$

The total excitonic population is defined as $\int \rho_{k,k}^e dk$, where $\rho_{k,k}^e$ is given by Eq. (C6). Substituting the obtained expressions for $\rho_{k\pm,k\pm}(0)$ into Eq. (C7) and (C6) and omitting the oscillating terms, $\propto \exp[-i(\varepsilon_{k\pm}-\varepsilon_{k\mp})t]$, we obtain

$$\overline{P_{ex}} = \int_{-\pi}^{\pi} P_k(0) [\cos^4(\theta_k) + \sin^4(\theta_k)] dk. \quad (\text{C11})$$

2. First and second moments

From Eq. (C2), the CM position is given in terms of the derivative with respect to k , $[\rho_{k,k}^e]'$

$$\begin{aligned} [\rho_{k,k}^e]'(t) &= \left[\frac{\partial e^{-i(\varepsilon_{k-}-\varepsilon_{k-+q})t}}{\partial q} \right]_{q=0} \\ &\quad \times \rho_{k-,k-}(0) \sin(\theta_k) \sin(\theta_k) \\ &\quad + \left[\frac{\partial}{\partial q} \rho_{k-,k-+q}(0) \sin(\theta_k) \sin(\theta_{k+q}) \right]_{q=0} + \dots \end{aligned} \quad (\text{C12})$$

where e.g.,

$$\left[\frac{\partial e^{-i(\varepsilon_{k-}-\varepsilon_{k-+q})t}}{\partial q} \right]_{q=0} = it \left[\frac{\partial \varepsilon_{k-+q}}{\partial q} \right]_{q=0} \equiv it \varepsilon'_{k-}. \quad (\text{C13})$$

Overall, we have

$$\begin{aligned} [\rho_{k,k}^e]'(t) &= it \varepsilon'_{k-} \rho_{k-,k-}(0) \sin(\theta_k) \sin(\theta_k) \\ &\quad + \left[\frac{\partial}{\partial q} \rho_{k-,k-+q}(0) \sin(\theta_k) \sin(\theta_{k+q}) \right]_{q=0} \\ &\quad + it \varepsilon'_{k+} e^{-i(\varepsilon_{k-}-\varepsilon_{k+})t} \rho_{k-,k+}(0) \sin(\theta_k) \cos(\theta_k) \\ &\quad + e^{-i(\varepsilon_{k-}-\varepsilon_{k+})t} \left[\frac{\partial}{\partial q} \rho_{k-,k+q}(0) \sin(\theta_k) \cos(\theta_{k+q}) \right]_{q=0} \\ &\quad + it \varepsilon'_{k-} e^{-i(\varepsilon_{k+}-\varepsilon_{k-})t} \rho_{k+,k-}(0) \cos(\theta_k) \sin(\theta_k) \\ &\quad + e^{-i(\varepsilon_{k+}-\varepsilon_{k-})t} \left[\frac{\partial}{\partial q} \rho_{k+,k-+q}(0) \cos(\theta_k) \sin(\theta_{k+q}) \right]_{q=0} \\ &\quad + it \varepsilon'_{k+} \rho_{k+,k+}(0) \cos(\theta_k) \cos(\theta_k) \\ &\quad + \left[\frac{\partial}{\partial q} \rho_{k+,k+q}(0) \cos(\theta_k) \cos(\theta_{k+q}) \right]_{q=0}. \end{aligned} \quad (\text{C14})$$

Considering the non-oscillating (and imaginary) terms proportional to t , we get

$$\begin{aligned} \overline{\langle n \rangle} &= -i \int [\rho_{k,k}^e]' dk \\ &= t \int_{-\pi}^{\pi} P_k(0) [\varepsilon'_{k+} \cos^4(\theta_k) + \varepsilon'_{k-} \sin^4(\theta_k)] dk, \end{aligned} \quad (\text{C15})$$

where we omitted the constant terms, since $\langle n(0) \rangle = 0$.

Similarly, for the second moment in Eq. (C3), we can evaluate the second derivative of $\rho_{k,k+q}^e$ with respect to q . Considering the non-oscillating (and real) terms proportional to t^2 (and omitting the constant term, corresponding to $\langle n^2(0) \rangle$), we obtain Eq. (14).

Appendix D: Stochastic multimode Tavis-Cummings model – Approximate Solution

Without the homogenizing terms [the last two terms in Eq. (18a)], the set of equation in Eq. (18) can be solved analytically using the Laplace transform method.

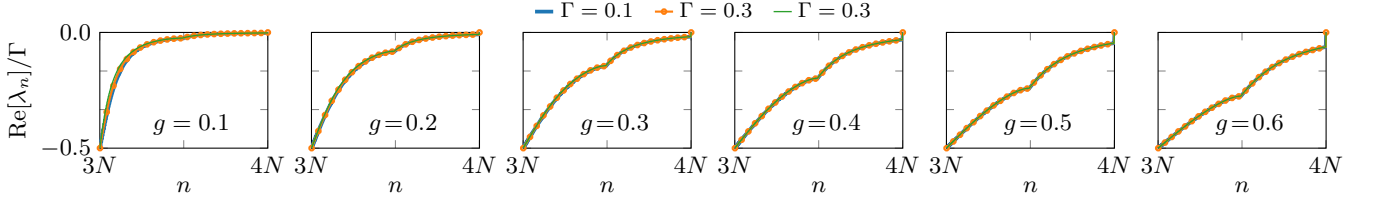


FIG. E1. N smallest real eigenvalues of the system in Eq. (18). Parameters: $\rho = 1$, $\omega_c = 0.4$, $g = 0.3$.

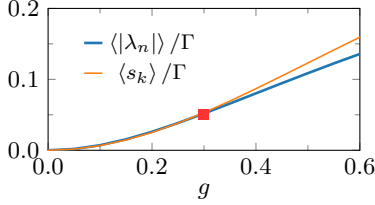


FIG. E2. Average of $N/2$ smallest real eigenvalues vs the averages in Eq. (E1). Parameters: $\rho = 1$, $\omega_c = 0.4$.

Assuming for simplicity that only the matter modes are initially populated (the initial state doesn't affect the characteristic frequencies and rates), we find the Laplace transform of $\rho_{k,k}^e(t)$

$$\tilde{\rho}_{k,k}^e(s) = \frac{1}{s} \frac{4g^2(\Gamma + 2s) + s(\Gamma + 2s)^2 + 4s\delta_k^2}{8g^2(\Gamma + 2s) + s(\Gamma + 2s)^2 + 4s\delta_k^2} P_k(0), \quad (\text{D1})$$

where $\delta_k \equiv \omega_k - \omega_{\text{eg}}$ is the detuning of mode k from the emitter transition frequency. Equation (D1) shows that the frequencies and decay rates of each $\rho_{k,k}^e(t)$ are given by the roots of the cubic polynomial

$$P_k(s) = 8g^2(\Gamma + 2s) + s(\Gamma + 2s)^2 + 4s\delta_k^2. \quad (\text{D2})$$

$P_k(s)$ has two complex roots (complex conjugates) that define the oscillation frequency of $\rho_{k,k}^e(t)$, and one real root [see Eq. (19)] that defines the purely decaying component.

Appendix E: Relaxation rate estimates

This Appendix considers additional examples of the eigenvalues of the system in Eq. (18). Figure E1 shows N smallest eigenvalues (scaled by Γ) for a range of Γ and g values. The figure confirms the eigenvalues' linear scaling with Γ for $\Gamma \leq 0.3$.

Figure E2 compares averages of $N/2$ eigenvalues from Fig. E1, $\langle |\lambda_n| \rangle / \Gamma$ and the average of TLS rates [Eq. (19)]

$$\frac{\langle s_k \rangle}{\Gamma} = \frac{1}{\pi/4} \int_{3\pi/4}^{\pi} \frac{2g^2 dk}{4g^2 + \delta_k^2}. \quad (\text{E1})$$

The integration limits were chosen to include the smallest TLS rates which are comparable to the $N/2$ smallest

eigenvalues. The red square denotes the point $g = 0.3$, where the effective rate is 0.05Γ , close to the value in Fig. 10(c).

Appendix F: Stretched exponential fit of the emitters' population

This Appendix presents the fitting results of the smoothed-out total excitonic population [Fig. 9(a,b)] using the model $a \exp(-\alpha t^\beta) + 1/2$. Figure F1 shows the fit parameters α and β as a function of Γ for several values of initial momentum, p . The stretching exponent β is approximately independent of Γ for $\Gamma > 0.05$, and the value is close to $2/3$. For the p and Γ values considered, the coefficient α scales approximately linearly with Γ .

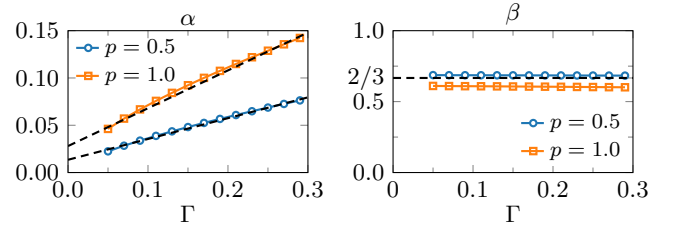


FIG. F1. Coefficient α (a) and stretching exponent β (b) as a function of Γ . Parameters: $\rho = 1$, $\omega_c = 0.4$, $g = 0.3$, $w = 10$. The black dashed lines are added to guide the eye.

Appendix G: Population relaxation rate estimation

This Appendix compares the relaxation rates of the total exciton population obtained from the full signal vs the smoothed-out signal, including only the contribution of the N smallest real eigenvalues [see Fig. 9(a,b)]. The relaxation rates are evaluated using the integral formula in Eq. (20).

Figure G1(a,b) shows the relaxation rates as a function of Γ . The rates from the full signal slightly deviate from the strictly linear Γ -dependence found for the smoothed-out signals. Figure G1(c) shows the relaxation rates as a function of p for several values of Γ . The rates obtained from the full signal are comparable with the rates of the smooth signal and exhibit roughly similar trends.

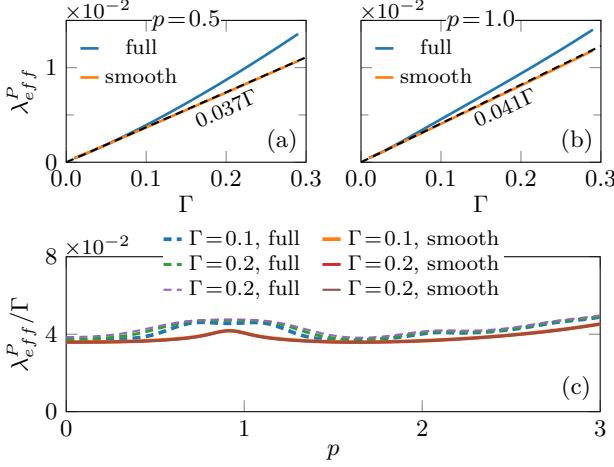


FIG. G1. Effective relaxation rate of the total excitonic population, P_{ex} , see Eq. (20). Rates obtained from the full signal vs. the smoothed-out signal are compared. Parameters: $\rho = 1$, $\omega_c = 0.4$, $g = 0.3$, $w = 10$.

Appendix H: Distribution moments from the reduced equations of motion for density matrix

Here, we outline our approach for calculating the first two moments of the emitters' population distribution using the reduced equations of motion for the density matrix elements in Eq. (18).

CM position.—The unnormalized CM position, $\langle n \rangle$ is given by an integral of the density matrix derivative, $\partial_q [\rho_{k,k+q}^e]_{q=0} \equiv [\rho_{k,k}^e]'$ in Eq. (11). Instead of deriving equations similar to those in Eq. (18) for $[\rho_{k,k}^e]'$, we can use a finite difference approximation for the first derivative, i.e., $[\rho_{k,k}^e]' \approx (\rho_{k,k+dq}^e - \rho_{k,k}^e)/dq$. By taking $dq \ll 1$,

$[\rho_{k,k}^e]'$ can be approximated with high precision. Moreover, since $\langle n \rangle$ and $\rho_{k,k}^e$ are real, we have

$$\langle n \rangle \approx \frac{1}{dq} \int \text{Im}[\rho_{k,k+dq}^e] dk. \quad (\text{H1})$$

This approach lets us obtain $\langle n \rangle$ by solving the system in Eq. (18) just once with $dq \ll 1$.

Second moment.—The second moment, $\langle n^2(t) \rangle$ can be expressed in terms of the second-order derivative of the density matrix, $\partial_q^2 [\rho_{k,k+q}^e]_{q=0} \equiv [\rho_{k,k}^e]''$ see Eq. (12). Using the same approach as for CM, $[\rho_{k,k}^e]''$ is approximated by

$$[\rho_{k,k}^e]'' \approx \frac{\rho_{k,k+dq}^e - 2\rho_{k,k}^e + \rho_{k,k-dq}^e}{(dq)^2} = \frac{2}{(dq)^2} (\text{Re}[\rho_{k,k+dq}^e] - \rho_{k,k}^e), \quad (\text{H2})$$

which allows computing the diffusivity by solving the system of equations in Eq. (18) only twice for $dq = 0$ and $dq \ll 1$.

ACKNOWLEDGMENTS

J.C. and I.T. acknowledge support from the NSF (Grants No. CHE1800301 and No. CHE2324300), and the MIT Sloan Fund. I.T. and H.R.S. acknowledge support from the NSF through a grant for ITAMP at Harvard University. M.Q. extends thanks to G. Engelhardt, L. Premkumar, and K. E. Dorfman and gratefully acknowledges the financial and computational support provided by the Beijing CSRC.

[1] G. Sandik, J. Feist, F. J. Garcia-Vidal, and T. Schwartz, Cavity-enhanced energy transport in molecular systems, *Nat. Mater.* **(2024)**.

[2] F. J. Garcia-Vidal, C. Ciuti, and T. W. Ebbesen, Manipulating matter by strong coupling to vacuum fields, *Science* **373** (2021).

[3] D. Sanvitto and S. Kéna-Cohen, The road towards polaritonic devices, *Nat. Mater.* **15**, 1061 (2016).

[4] M. Son, Z. T. Armstrong, R. T. Allen, A. Dhavamani, M. S. Arnold, and M. T. Zanni, Energy cascades in donor-acceptor exciton-polaritons observed by ultrafast two-dimensional white-light spectroscopy, *Nat. Commun.* **13**, 7305 (2022).

[5] C. A. DelPo, S.-U.-Z. Khan, K. H. Park, B. Kudisch, B. P. Rand, and G. D. Scholes, Polariton Decay in Donor-Acceptor Cavity Systems, *J. Phys. Chem. Lett.* **12**, 9774 (2021).

[6] G. Lerario, D. Ballarini, A. Fieramosca, A. Cannavale, A. Genco, F. Mangione, S. Gambino, L. Dominici, M. De Giorgi, G. Gigli, and D. Sanvitto, High-speed flow of interacting organic polaritons, *Light Sci. Appl.* **6**, e16212 (2017).

[7] X. Zhong, T. Chervy, S. Wang, J. George, A. Thomas, J. A. Hutchison, E. Devaux, C. Genet, and T. W. Ebbesen, Non-Radiative Energy Transfer Mediated by Hybrid Light-Matter States, *Angew. Chem. Int. Ed. Engl.* **55**, 6202 (2016).

[8] D. M. Coles, N. Somaschi, P. Michetti, C. Clark, P. G. Lagoudakis, P. G. Savvidis, and D. G. Lidzey, Polariton-mediated energy transfer between organic dyes in a strongly coupled optical microcavity, *Nat. Mater.* **13**, 712 (2014).

[9] R. Sáez-Blázquez, J. Feist, A. I. Fernández-Domínguez, and F. J. García-Vidal, Organic polaritons enable local vibrations to drive long-range energy transfer, *Phys. Rev. B* **97**, 241407 (2018).

[10] M. Du, L. A. Martínez-Martínez, R. F. Ribeiro, Z. Hu, V. M. Menon, and J. Yuen-Zhou, Theory for polariton-assisted remote energy transfer, *Chem. Sci.* **9**, 6659 (2018).

[11] M. Reitz, F. Mineo, and C. Genes, Energy transfer and correlations in cavity-embedded donor-acceptor configurations, *Sci. Rep.* **8**, 9050 (2018).

[12] J. Cao, Generalized Resonance Energy Transfer Theory: Applications to Vibrational Energy Flow in Optical Cavities, *J. Phys. Chem. Lett.* **13**, 10943 (2022).

[13] T. Khazanov, S. Gunasekaran, A. George, R. Lomlu, S. Mukherjee, and A. J. Musser, Embrace the darkness: An experimental perspective on organic exciton-polaritons, *Chem. Phys. Rev.* **4**, 041305 (2023).

[14] R. H. Tichauer, I. Sokolovskii, and G. Groenhof, Tuning the coherent propagation of organic exciton-polaritons through the cavity q-factor, *Adv. Sci.* **10**, 2302650 (2023).

[15] S. Hou, M. Khatoniar, K. Ding, Y. Qu, A. Napolov, V. M. Menon, and S. R. Forrest, Ultralong-range energy transport in a disordered organic semiconductor at room temperature via coherent exciton-polariton propagation, *Adv. Mat.* **32**, 2002127 (2020).

[16] G. G. Rozenman, K. Akulov, A. Golombek, and T. Schwartz, Long-range transport of organic exciton-polaritons revealed by ultrafast microscopy, *ACS Photonics* **5**, 105 (2018).

[17] J. Wenus, R. Parashkov, S. Ceccarelli, A. Brehier, J.-S. Lauret, M. S. Skolnick, E. Deleporte, and D. G. Lidzey, Hybrid organic-inorganic exciton-polaritons in a strongly coupled microcavity, *Phys. Rev. B* **74**, 235212 (2006).

[18] B. Liu, X. Huang, S. Hou, D. Fan, and S. R. Forrest, Photocurrent generation following long-range propagation of organic exciton-polaritons, *Optica* **9**, 1029 (2022).

[19] N. Krainova, A. J. Grede, D. Tsokkou, N. Banerji, and N. C. Giebink, Polaron Photoconductivity in the Weak and Strong Light-Matter Coupling Regime, *Phys. Rev. Lett.* **124**, 177401 (2020).

[20] K. Nagarajan, J. George, A. Thomas, E. Devaux, T. Chervy, S. Azzini, K. Joseph, A. Jouaiti, M. W. Hosseini, A. Kumar, C. Genet, N. Bartolo, C. Ciuti, and T. W. Ebbesen, Conductivity and Photoconductivity of a p-Type Organic Semiconductor under Ultrastrong Coupling, *ACS Nano* **14**, 10219 (2020).

[21] E. Orgiu, J. George, J. A. Hutchison, E. Devaux, J. F. Dayen, B. Doudin, F. Stellacci, C. Genet, J. Schachenmayer, C. Genes, G. Pupillo, P. Samori, and T. W. Ebbesen, Conductivity in organic semiconductors hybridized with the vacuum field, *Nat. Mater.* **14**, 1123 (2015).

[22] T. E. Li, B. Cui, J. E. Subotnik, and A. Nitzan, Molecular polaritonics: Chemical dynamics under strong light-matter coupling, *Annu. Rev. Phys. Chem.* **73**, 43 (2022).

[23] R. F. Ribeiro, L. A. Martínez-Martínez, M. Du, J. Campos-Gonzalez-Angulo, and J. Yuen-Zhou, Polariton chemistry: controlling molecular dynamics with optical cavities, *Chem. Sci.* **9**, 6325 (2018).

[24] F. Herrera and F. C. Spano, Cavity-controlled chemistry in molecular ensembles, *Phys. Rev. Lett.* **116**, 238301 (2016).

[25] I. Tutunnikov, C. Chuang, and J. Cao, Coherent Spatial Control of Wave Packet Dynamics on Quantum Lattices, *J. Phys. Chem. Lett.* **14**, 11632 (2023).

[26] A. Amir, Y. Lahini, and H. B. Perets, Classical diffusion of a quantum particle in a noisy environment, *Phys. Rev. E* **79**, 050105 (2009).

[27] A. Buend'ia, J. A. Sánchez-Gil, V. Giannini, W. L. Barnes, and M. S. Rider, Long-range molecular energy transfer mediated by strong coupling to plasmonic topological edge states, *Nanophotonics* **14** (2024).

[28] G. J. R. Aroeira, K. T. Kairys, and R. F. Ribeiro, Theoretical Analysis of Exciton Wave Packet Dynamics in Polaritonic Wires, *J. Phys. Chem. Lett.* **14**, 5681 (2023).

[29] K. B. Arnardottir, A. J. Moilanen, A. Strashko, P. Törmä, and J. Keeling, Multimode organic polariton lasing, *Phys. Rev. Lett.* **125**, 233603 (2020).

[30] D. Hagenmüller, J. Schachenmayer, S. Schütz, C. Genes, and G. Pupillo, Cavity-enhanced transport of charge, *Phys. Rev. Lett.* **119**, 223601 (2017).

[31] C. Gonzalez-Ballester, J. Feist, E. Moreno, and F. J. Garcia-Vidal, Harvesting excitons through plasmonic strong coupling, *Phys. Rev. B* **92**, 121402 (2015).

[32] J. Feist and F. J. Garcia-Vidal, Extraordinary exciton conductance induced by strong coupling, *Phys. Rev. Lett.* **114**, 196402 (2015).

[33] J. Schachenmayer, C. Genes, E. Tignone, and G. Pupillo, Cavity-enhanced transport of excitons, *Phys. Rev. Lett.* **114**, 196403 (2015).

[34] G. Engelhardt and J. Cao, Unusual dynamical properties of disordered polaritons in microcavities, *Phys. Rev. B* **105**, 064205 (2022).

[35] G. Engelhardt and J. Cao, Polariton Localization and Dispersion Properties of Disordered Quantum Emitters in Multimode Microcavities, *Phys. Rev. Lett.* **130**, 213602 (2023).

[36] M. Balasubrahmanyam, A. Simkhovich, A. Golombek, G. Sandik, G. Ankonina, and T. Schwartz, From enhanced diffusion to ultrafast ballistic motion of hybrid light-matter excitations, *Nat. Mater.* **22**, 338 (2023).

[37] L. Jin, A. D. Sample, D. Sun, Y. Gao, S. Deng, R. Li, L. Dou, T. W. Odom, and L. Huang, Enhanced two-dimensional exciton propagation via strong light-matter coupling with surface lattice plasmons, *ACS Photonics* **10**, 1983 (2023).

[38] D. Xu, A. Mandal, J. M. Baxter, S.-W. Cheng, I. Lee, H. Su, S. Liu, D. R. Reichman, and M. Delor, Ultrafast imaging of polariton propagation and interactions, *Nat. Commun.* **14**, 3881 (2023).

[39] R. Pandya, A. Ashoka, K. Georgiou, J. Sung, R. Jayaprakash, S. Renken, L. Gai, Z. Shen, A. Rao, and A. J. Musser, Tuning the coherent propagation of organic exciton-polaritons through dark state delocalization, *Adv. Sci.* **9**, 2105569 (2022).

[40] R. H. Dicke, Coherence in spontaneous radiation processes, *Phys. Rev.* **93**, 99 (1954).

[41] M. Tavis and F. W. Cummings, Exact Solution for an *N*-Molecule–Radiation-Field Hamiltonian, *Phys. Rev.* **170**, 379 (1968).

[42] J. M. Moix, M. Khasin, and J. Cao, Coherent quantum transport in disordered systems: I. The influence of dephasing on the transport properties and absorption spectra on one-dimensional systems, *New J. Phys.* **15**, 085010 (2013).

[43] I. Tutunnikov and J. Cao, Unusual diffusivity in strongly disordered quantum lattices: Random dimer model, *arXiv:2405.20813 [quant-ph]* (2024).

[44] V. M. Agranovich, M. Litinskaya, and D. G. Lidzey, Cavity polaritons in microcavities containing disordered organic semiconductors, *Phys. Rev. B* **67**, 085311 (2003).

[45] M. Litinskaya, P. Reineker, and V. M. Agranovich, Fast polariton relaxation in strongly coupled organic microcavities, *J. Lumin.* **110**, 364 (2004).

[46] A. Strashko, P. Kirton, and J. Keeling, Organic Polariton Lasing and the Weak to Strong Coupling Crossover,

Phys. Rev. Lett. **121**, 193601 (2018).

[47] I. Sokolovskii, R. H. Tichauer, D. Morozov, J. Feist, and G. Groenhof, Multi-scale molecular dynamics simulations of enhanced energy transfer in organic molecules under strong coupling, *Nat. Commun.* **14**, 6613 (2023).

[48] V. A. Osipov and B. Fainberg, Hartree method for molecular polaritons, *Phys. Rev. B* **107**, 075404 (2023).

[49] A. M. Alvertis, R. Pandya, C. Quarti, L. Legrand, T. Barisien, B. Monserrat, A. J. Musser, A. Rao, A. W. Chin, and D. Beljonne, First principles modeling of exciton-polaritons in polydiacetylene chains, *J. Chem. Phys.* **153**, 084103 (2020).

[50] C. Schäfer, M. Ruggenthaler, H. Appel, and A. Rubio, Modification of excitation and charge transfer in cavity quantum-electrodynamical chemistry, *Proc. Natl Acad. Sci. USA* **116**, 4883 (2019).

[51] G. J. R. Aroeira, K. T. Kairys, and R. F. Ribeiro, Coherent transient exciton transport in disordered polaritonic wires, *Nanophotonics* **13**, 2553 (2024).

[52] C. K. Lee, J. Moix, and J. Cao, Coherent quantum transport in disordered systems: A unified polaron treatment of hopping and band-like transport, *J. Chem. Phys.* **142**, 164103 (2015).

[53] M. Berberan-Santos, E. Bodunov, and B. Valeur, Mathematical functions for the analysis of luminescence decays with underlying distributions 1. Kohlrausch decay function (stretched exponential), *Chem. Phys.* **315**, 171 (2005).

[54] C. Chuang, C. K. Lee, J. M. Moix, J. Knoester, and J. Cao, Quantum Diffusion on Molecular Tubes: Universal Scaling of the 1D to 2D Transition, *Phys. Rev. Lett.* **116**, 196803 (2016).

[55] J. Cao and R. J. Silbey, Optimization of exciton trapping in energy transfer processes, *J. Phys. Chem. A* **113**, 13825 (2009).

[56] H. L. Luk, J. Feist, J. J. Toppari, and G. Groenhof, Multiscale Molecular Dynamics Simulations of Polaritonic Chemistry, *J. Chem. Theory Comput.* **13**, 4324 (2017).

[57] R. Crespo-Otero and M. Barbatti, Recent Advances and Perspectives on Nonadiabatic Mixed Quantum-Classical Dynamics, *Chem. Rev.* **118**, 7026 (2018).

[58] M. K. Svendsen, K. S. Thygesen, A. Rubio, and J. Flick, Ab Initio Calculations of Quantum Light-Matter Interactions in General Electromagnetic Environments, *J. Chem. Theory Comput.* **20**, 926 (2024).

[59] D. Xu and J. Cao, Non-canonical distribution and non-equilibrium transport beyond weak system-bath coupling regime: A polaron transformation approach, *Front. Phys.* **11**, 1 (2016).

[60] T. F. Allard and G. Weick, Disorder-enhanced transport in a chain of lossy dipoles strongly coupled to cavity photons, *Phys. Rev. B* **106**, 245424 (2022).

[61] M. Anzola, C. Sissa, A. Painelli, A. A. Hassanali, and L. Grisanti, Understanding Förster Energy Transfer through the Lens of Molecular Dynamics, *J. Chem. Theory Comput.* **16**, 7281 (2020).